Weak-strong beam-beam simulations for the LHC

Y. Papaphilippou and F. Zimmermann, CERN, Geneva, Switzerland

Abstract

A weak-strong simulation code similar to the one written by Irwin for the Superconducting Super Collider (SSC) [1] is used to study the single-particle stability in the presence of triplet field errors, head-on collisions and long-range beam-beam interactions at the Large Hadron Collider (LHC). We present the dependence of the simulated transverse diffusion rate on various parameters, such as starting amplitude, working point in tune diagram, crossing angle, beta function at the interaction points (IPs), beam current, triplet nonlinearities, tune modulation and a transverse offset at one of the two IPs. For several examples, we perform a frequency map analysis à la Laskar, to obtain tune footprints and the tune variation in time. A cursory look at the effect of a Möbius lattice is also reported.

1 INTRODUCTION

The long-range force is expected to become important for amplitudes where particles pass near the center of the opposing beam at the parasitic collision points. Using this criterion, a diffusive aperture can be estimated as

$$x_{da} \approx \frac{\theta_c}{\theta_x}\,\sigma_x\ , \qquad (1)$$

where θ_c denotes the full crossing angle, θ_x the rms divergence, and σ_x the rms beam size at the IP. For the nominal LHC parameters, listed in Table 1, x_{da} amounts to about 9.5 σ_x. Simulation studies showed that, in the presence of tune modulation, the diffusive aperture of the SSC was actually about 2.5 σ_x smaller, a reduction which was found to be independent of the crossing angle [1]. Hence, extrapolating from these results we would predict the LHC diffusive aperture at about 7 σ_x. However, the LHC and SSC parameters differ substantially, e.g. the SSC bunch population was only 7.3×10^9, 15 times less than that of the LHC. Thus, a simple extrapolation may not be valid. In addition, since the beam-beam interaction is the most important limitation of the LHC performance at top energy, it is important to study the effect on the beam stability of various related parameters, such as the beam current, the beams' crossing angle or the IP beta function, whose values have a direct impact on the luminosity.

Here, we report the results of a dedicated simulation study for the LHC.[1] The paper is organised as follows. In Section 2, we describe the employed weak-strong model. Section 3 presents the simulation results. We summarise and conclude in Section 4.

parameter	symbol	value
particles per bunch	N_b	1.05×10^{11}
beam energy	E_b	7 TeV
rms beam size at IP	$\sigma_{x,y}$	16μm
rms divergence at IP	$\theta_{x,y}$	31.7 μrad
IP beta function	$\beta^\star_{x,y}$	50 cm
full crossing angle	θ_c	300 μrad
rms bunch length	σ_z	7.7 cm
collision points	n_{IP}	≥ 2
bunches per beam	n_b	2835
bunch spacing	L_{sep}	7.48 m
beam-beam parameter	ξ	0.00342
revolution frequency	f_{rev}	11.25 kHz
synchrotron tune	Q_s	0.00212
luminosity per collision	L_{coll}	3.14×10^{26} cm^{-2}
total luminosity	L_{tot}	10^{34} cm^{-2} s^{-1}

Table 1: LHC collision parameters [2].

2 MODEL

The simulation study was performed following the recipe given by Irwin [1], and using the LHC parameters of Table 1. The simulation is 4-dimensional: the horizontal and vertical motion of single particles is calculated under the influence of the field of the opposing beam. An optional tune modulation can also be selected. We treat two IPs, symmetrically spaced around the ring, one with a horizontal crossing angle, the other with a vertical crossing angle, so that the linear tune shifts induced by the long-range interactions cancel between the IPs. At each IP, we apply a series of five kicks: the first represents the lumped effect of the triplet nonlinearities, the next corresponds to the long-range beam-beam interactions on the incoming side; then a kick for the head-on collision effect is applied, another for the long-range interaction on the outgoing side, and finally a kick due to the triplet nonlinearities on the outgoing side. These tracking elements are described now in more detail.

[1] Note that similar dynamic aperture studies were performed earlier by Ritson and Chou [3].

order n	mean $b_{n,M}$	uncertainty $b_{n,U}$	rms $b_{n,rms}$	mean $a_{n,M}$	uncertainty $a_{n,U}$	rms $a_{n,rms}$
3	0.	0.3	0.8	0.	0.3	0.8
4	0.	0.2	0.8	0.	0.2	0.8
5	0.	0.2	0.3	0.	0.2	0.3
6	0.14	0.6	0.7	0.	0.085	0.11
7	0.	0.05	0.06	0.	0.04	0.06
8	0.	0.03	0.05	0.	0.03	0.04
9	0.	0.02	0.03	0.	0.02	0.02
10	-0.027	0.02	0.043	0.	0.027	0.037

Table 2: Harmonic multipole content in low-β quadrupoles (Fermilab Design), after application of tuning shim correction [5, 6]. The harmonic values are quoted in units of 10^{-4} of the main quadrupole field, for a reference radius $r_0 = 17$ mm. The uncertainty in the mean, as well as the estimated standard deviation are also listed.

2.1 Arcs

Between the two IPs, denoted by sub-indices i and j, we perform a linear rotation of the form

$$\begin{pmatrix} x \\ x' \\ y \\ y' \end{pmatrix}_{IPi} = \mathcal{R}_{ij} \begin{pmatrix} x \\ x' \\ y \\ y' \end{pmatrix}_{IPj} , \qquad (2)$$

with the rotation matrix

$$\mathcal{R}_{ij} = \begin{pmatrix} \cos\phi_x & \beta_x^\star \sin\phi_x & 0 & 0 \\ -\frac{1}{\beta_x^\star}\sin\phi_x & \cos\phi_x & 0 & 0 \\ 0 & 0 & \cos\phi_y & \beta_y^\star \sin\phi_y \\ 0 & 0 & -\frac{1}{\beta_y^\star}\sin\phi_y & \cos\phi_y \end{pmatrix} . \qquad (3)$$

The coordinates are those at the successive IPs and primes denote the particle slopes. Unless noted otherwise, we assume that the two rotation matrices, from IP 1 to IP 2 and from IP 2 to IP 1, are identical (*i.e.* $\mathcal{R}_{12} = \mathcal{R}_{21}$), and also that the beta functions at the interaction points, $\beta_x^\star$ and $\beta_y^\star$, are the same in both planes and at both IPs and equal to the LHC design value $\beta_x^\star = \beta_y^\star = 0.5$ m. The bare half-ring phase advances were chosen as $\phi_x = 2 \times \pi \times 31.655$, and $\phi_y = 2 \times \pi \times 29.66$, corresponding to the nominal working point of LHC optics version 5.

2.2 Head-On Collision

For the beam-beam interaction we assume round Gaussian beam profiles. The effect of head-on collisions is then given by

$$\begin{aligned} \Delta x' &= \frac{2 r_p N_b}{\gamma} \frac{x}{r^2} \left(1 - e^{-\frac{r^2}{2\sigma^2}}\right) \\ \Delta y' &= \frac{2 r_p N_b}{\gamma} \frac{y}{r^2} \left(1 - e^{-\frac{r^2}{2\sigma^2}}\right) \end{aligned} , \qquad (4)$$

with $\sigma \equiv \sigma_x = \sigma_y$ the rms beam size at the IP, $r = \sqrt{x^2 + y^2}$ the radial distance to the origin, r_p the classical proton radius, γ the Lorentz factor, and N_b the bunch population.

2.3 Long-Range Interactions

For the long-range interactions, we lump together the effect of all n_{par} parasitic collisions on each side of the IP. Since they occur at a betatron phase close to $\pi/2$, the kick can be approximately expressed as a change in the IP coordinate, while the trajectory slope at the IP stays unchanged. In case of a horizontal crossing we have:

$$\begin{aligned} \Delta x = &- n_{par} \frac{2 r_p N_b}{\gamma} \left[\frac{x' + \theta_c}{\theta_t^2} \left(1 - e^{-\frac{\theta_t^2}{2\theta_{x,y}^2}}\right) \right. \\ &\left. - \frac{1}{\theta_c} \left(1 - e^{-\frac{\theta_c^2}{2\theta_{x,y}^2}}\right) \right] , \qquad (5) \\ \Delta y = &- n_{par} \frac{2 r_p N_b}{\gamma} \frac{y'}{\theta_t^2} \left(1 - e^{-\frac{\theta_t^2}{2\theta_{x,y}^2}}\right) \end{aligned}$$

where $\theta_t \equiv \left((x' + \theta_c)^2 + y'^2\right)^{1/2}$ and $\theta_{x,y}$ is the rms beam divergence at the IP. The effective number of parasitic crossings per side of one IP, n_{par}, is about 18 [4]. In the first part of Eq. (5), we subtract the average horizontal dipole kick on the bunch, since its effect would be corrected by steering correctors. Note that the kick is the same on both sides of the IP, because the betatron phase advance of about 180° compensates for the opposite direction of the beam-beam separation. The vertical crossing is treated in complete analogy.

2.4 Triplet Nonlinearities

The integrated effect of the higher-order multipoles in the low-β quadrupoles can be written in complex form. Under some simplifying assumptions (equal β functions in the two transverse planes), the nonlinear kick on the incoming

order n	mean $b_{n,M}$	uncertainty $b_{n,U}$	rms $b_{n,rms}$	mean $a_{n,M}$	uncertainty $a_{n,U}$	rms $a_{n,rms}$
3	0.	0.51	1.	0.	0.51	1.
4	0.	0.29	0.57	0.	0.29	0.57
5	0.	0.19	0.38	0.	0.19	0.38
6	0.38	0.5	0.19	0.01	0.1	0.19
7	0.	0.05	0.06	0.	0.05	0.06
8	0.	0.02	0.03	0.	0.02	0.03
9	0.	0.01	0.01	0.	0.01	0.01
10	0.22	0.03	0.01	-0.003	0.01	0.01

Table 3: Harmonic multipole content in low-β quadrupoles (KEK Design) [6, 7]. The harmonic values are quoted in units of 10^{-4} of the main quadrupole field, for a reference radius $r_0 = 17$ mm.

side of the IP with horizontal crossing is given by

$$\Delta x = -\bar{K}\ \mathrm{Re}\left[\sum_{n=3}^{n_{max}} \mathcal{G}_n\Big(-\frac{1}{r_0}\Big)^{n-1}\left(\Big(x' + \frac{\theta_c}{2} + iy'\Big)^{n-1} - (n-1)\Big(\frac{\theta_c}{2}\Big)^{n-2}(x'+iy') - \Big(\frac{\theta_c}{2}\Big)^{n-1}\right)\right]$$

$$\Delta y = \bar{K}\ \mathrm{Im}\left[\sum_{n=3}^{n_{max}} \mathcal{G}_n\Big(-\frac{1}{r_0}\Big)^{n-1}\left(\Big(x' + \frac{\theta_c}{2} + iy'\Big)^{n-1} - (n-1)\Big(\frac{\theta_c}{2}\Big)^{n-2}(x'+iy') - \Big(\frac{\theta_c}{2}\Big)^{n-1}\right)\right], \tag{6}$$

where the complex coefficient $\mathcal{G}_n$ represents the effective strength of the nth order multipole kick, through the sum

$$\mathcal{G}_n = \beta_{x,y}^{\star\ n/2}\left(\sum_{k=1}^{4}(a_{n,k} + ib_{n,k})\beta_k^{n/2}\right)$$

over the 4 low-beta quadrupoles on one side of the IP. The latter expression is evaluated prior to the tracking, with β_k the geometric mean of the horizontal and vertical beta function at the center of the kth quadrupole, and $a_{n,k}$ and $b_{n,k}$ the skew and normal multipole components relative to the main quadrupole field at the same reference radius r_0 (see Tables 2 and 3). The coefficient $\bar{K}$ in Eq. (6) is equal to $\bar{K} = l_{quad}\ r_0\ K_1$, where l_{quad} denotes the quadrupole length ($l_{quad} \approx 5$ m) and K_1 the non-integrated quadrupole gradient ($K_1 \approx 0.01$ m^{-2}). As before, x' and y' are the trajectory slopes at the IP. Note that the dipole kick as well as the static quadrupole and skew quadrupole components induced by the crossing angle are subtracted, because we assume that in the real machine the changes in the closed orbit, tunes and coupling, due to the field errors, will all be corrected by standard tuning methods. This could be a difference with respect to previous applications of similar kick-map codes for the SSC and the LHC [1, 3].

For the outgoing side, we use the same formulae, but without the "$-$" sign in $(\frac{1}{r_0})^{n-1}$. This means that the net effect of the systematic field errors of even order n would cancel if there were no head-on collisions at the IP. Finally, the case of the vertical crossing is treated identically except that $\theta_c/2$ is added to y' instead of x'.

In the present study, we consider a single random seed for the errors calculated according to Tables 2 and 3.

2.5 *Tune Modulation*

As a further ingredient in our simulation a tune modulation can be added. It is described by a linear transport matrix of the form

$$\mathcal{M} = \begin{pmatrix} \cos\Delta\phi_x & \beta_x^\star \sin\Delta\phi_x & 0 & 0 \\ \frac{-1}{\beta_x^\star}\sin\Delta\phi_x & \cos\Delta\phi_x & 0 & 0 \\ 0 & 0 & \cos\Delta\phi_y & \beta_y^\star\sin\Delta\phi_y \\ 0 & 0 & \frac{-1}{\beta_y^\star}\sin\Delta\phi_y & \cos\Delta\phi_y \end{pmatrix}, \tag{7}$$

where

$$\begin{aligned} \Delta\phi_x &= 2\pi\ \Delta Q_x \sin(2\pi f_x t) \\ \Delta\phi_y &= 2\pi\ \Delta Q_y \sin(2\pi f_y t) \end{aligned}.$$

Here, $\Delta Q_{x,y}$ and $f_{x,y}$ denote the modulation amplitude and frequency, respectively, and t is the time. For instance, synchrotron oscillations and residual chromaticity result in a modulation of the betatron tune for off-energy particles. Assuming $Q' \approx 1$, a particle at $1\sigma_\delta$ experiences an effective tune modulation of amplitude 10^{-4} at the 22 Hz synchrotron frequency. Ground motion, magnet vibrations, and power supply ripple may also induce tune modulation at similar amplitudes and frequencies.

2.6 *Möbius Insertion*

In addition, a Möbius transformation [8] may be inserted, in order to study the stabilising, or destabilising, properties of such a scheme. The Möbius twist is of the simple form:

$$\begin{pmatrix} x \\ x' \\ y \\ y' \end{pmatrix}_{IPi} = \begin{pmatrix} 0 & 0 & -1 & 0 \\ 0 & 0 & 0 & -1 \\ -1 & 0 & 0 & 0 \\ 0 & -1 & 0 & 0 \end{pmatrix} \begin{pmatrix} x \\ x' \\ y \\ y' \end{pmatrix}_{IPj}. \tag{8}$$

Because of the additional symmetry of a Möbius lattice, there is only one independent tune value. The two tune lines, $Q_\pm$, are placed symmetrically above and below 0.25:

$$Q_\pm = Q_x + Q_y \pm 0.25 \tag{9}$$

where Q_x and Q_y denote the nominal tunes without the Möbius twist.

3 RESULTS

3.1 Tune Footprints and Diffusion Maps

Frequency map analyses have long been used in celestial mechanics and recently in accelerator models [10, 11]. In this section we present results from an application of this technique to the beam-beam interaction, through the kick-map model discussed previously.

Figure 1 presents tune footprints à la Laskar [10, 11], obtained by tracking single particles over 1000 turns and, subsequently, frequency analysing the tracking data with the SUSSIX program [9]. Through this analysis, we compute with a very high precision [12] the fundamental frequencies of motion, for a large number of initial conditions, with initial horizontal and vertical amplitudes varying from 0 to 10 $\sigma_{x,y}$, and initial slopes set to zero. By plotting the fundamental frequencies in tune space, phase-space distortions representing resonances or chaotic regions become visible.

The dramatic effect of the long-range collisions is revealed through the comparison of Figs. 1b and a, which show footprints obtained with and without the long-range kicks. Up to initial particle amplitudes of around $6\sigma_{x,y}$, the effect of the head-on collisions dominates. Then, the long-range effect takes over and the frequency footprint flips, as the tune shift with amplitude changes direction. This non-monotonic dependence of the tune with respect to the amplitude is potentially dangerous for the stability of particles beyond this limit.

The additional detrimental influence of the triplet non-linearities can be observed in the plots 1c and d, where we include the effect of the errors in the quadrupoles designed in FNAL and KEK, respectively. The tune shift with amplitude gets larger and the difference resonances of order 5 and above are getting more pronounced. From this representation, however, it is difficult to say which of the two type of magnet families is more harmful with respect to the beam stability.

The two remaining images 1e and f show the pure effect of the KEK triplet errors and the combined influence of triplet errors and parasitic collisions, respectively. It is clear, that the long-range effect is dominant. Indeed, the tune spread induced for amplitudes up to $10\sigma_{x,y}$ is of similar size as with the head-on collisions included (compare Figs. 1b and f).

In all the cases, except the one with head-on collisions only, some particles diffuse out to the $(1, -1)$ resonance, as our working point is quite close to the frequency space diagonal.

An additional outcome of the frequency map analysis is displayed in the plots of Fig. 2, where we depict the variation of the betatron tunes $|\Delta\mathbf{Q}|$ that occurs between the first and second sets of 500 turns, as a function of the starting amplitude [10, 11]. The different colours correspond to different amounts of tune variation on a logarithmic scale, extending from $|\Delta\mathbf{Q}| \leq 10^{-7}$ to $|\Delta\mathbf{Q}| > 10^{-2}$. The grey regions correspond to particles with a tune variation less than or equal to the precision of the tune calculation for this number of turns. Thus, their tune variation is consistent with no variation at all, and they may be considered as completely stable. The two types of green areas are weakly unstable. We speculate that the blue, magenta and brown regions are strongly chaotic, and that particles in the black areas also might be lost, after a larger number of turns. In these plots we can observe directly the traces of resonances which limit the region of stability. The conclusions of the previous paragraph regarding the dominant destabilising role of the long-range collisions are also confirmed here. The additional effect of head-on collisions and triplet non-linear fields is negligible.

A further frequency analysis was performed for a model with a reduced crossing angle of 200 μrad (Fig. 3). The two images can be directly compared to Figs. 2d and 1d, which correspond to the same model, but at the nominal crossing angle (300 μrad). For the smaller crossing angle, the diffusive aperture should be diminished, according to Eq. (1). Indeed, the tune shift with amplitude is further increased (Fig. 3a) and the particle motion is heavily perturbed at amplitudes beyond about $4\sigma_{x,y}$ (Fig. 3b).

The influence of the application of a Möbius twist (8) to the phase space of the system is presented in the diffusion map of Fig. 4. In that case, tune footprints cannot be provided, as there is only one independent tune. The diffusion map now presents features which are symmetric with respect to the diagonal of the initial amplitude space. It seems that by this twist, instead of stabilising the system, we mirror instabilities in other parts of the phase space. This was also reported in a recent experimental study [13].

An illustrative comparison of the phase space stability for all the previous cases is given in Fig. 5. We plot the average tune difference in logarithmic scale over all the tracked particles. The two curves correspond to a simple average of the tune change and another average of the tune variation normalised by the particles' initial amplitudes. The head-on case presents the smallest tune diffusion coefficient. By just adding the long-range the coefficient jumps by two orders of magnitude. The addition of triplet non-linearities further perturbs the system and we can even distinguish a small difference between the case with FNAL and KEK design triplets. Interestingly enough, the case without head-on but with long-range and triplet errors seems more unstable: the linear tune shift due to the head-on effect puts the tune to a position further away from the dangerous $(0, 3)$ skew resonance. The situation, as we have seen before will get worse by diminishing the crossing angle to 200 μrad or by including a Möbius twist [13].

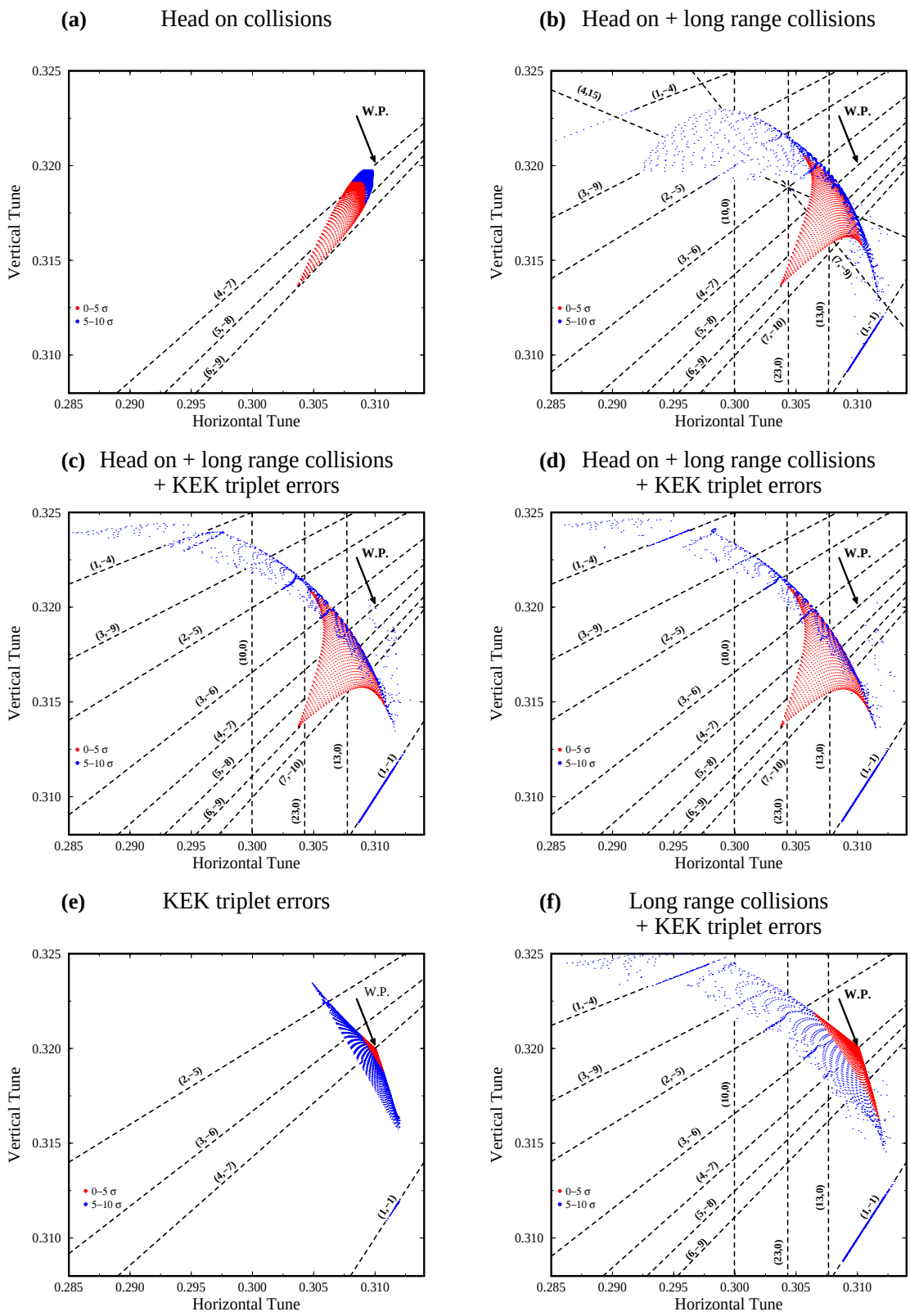

Figure 1: Tune footprints obtained by tracking single particles over 1000 turns and subsequent analysis with SUSSIX. Red dots represent particles with initial transverse amplitudes up to $5\sigma_{x,y}$; blue dots show results for an extended range with initial amplitudes up to 10 $\sigma_{x,y}$; **(a)** head-on collisions only, **(b)** head-on and long-range collisions **(c)** head-on plus long-range collisions and FNAL triplet errors (1 random seed) **(d)** head-on plus long-range collisions and KEK triplet errors (1 random seed), **(e)** KEK triplet errors only (1 random seed), **(f)** long-range collisions and KEK triplet errors (1 random seed), but no head-on collisions.

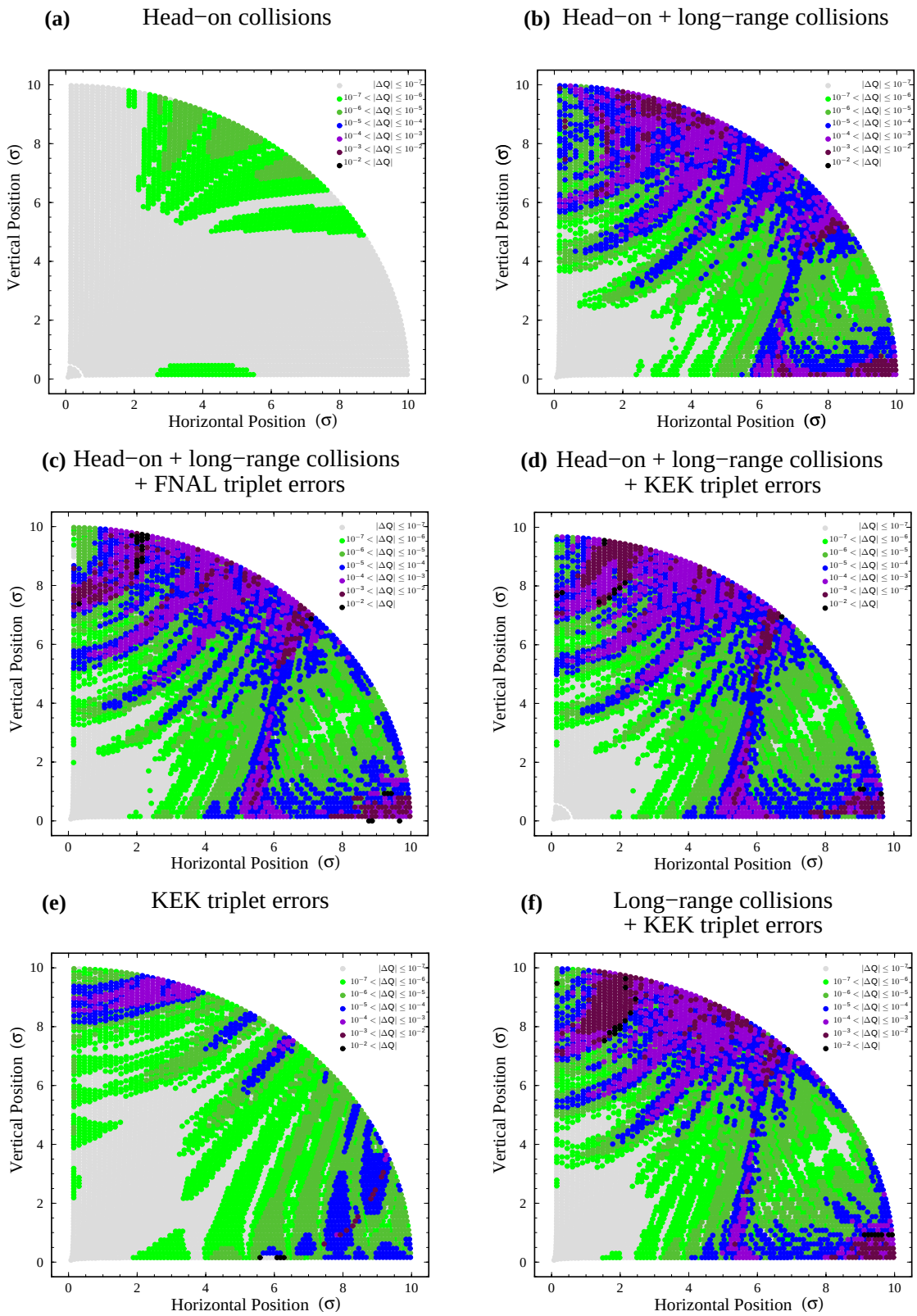

Figure 2: Diffusion maps representing the change of the betatron tunes with time as a function of horizontal and vertical starting amplitude. The tune change was inferred by tracking single particles over 2 times 500 turns and subsequent analysis with SUSSIX. The colour assignment is logarithmically scaled with the tune change $|\Delta Q|$ over 500 turns; **(a)** head-on collisions only, **(b)** head-on and long-range collisions **(c)** head-on plus long-range collisions and FNAL triplet errors (1 random seed) **(d)** head-on plus long-range collisions and KEK triplet errors (1 random seed), **(e)** KEK triplet errors only (1 random seed), **(f)** long-range collisions and KEK triplet errors (1 random seed), but no head-on collisions.

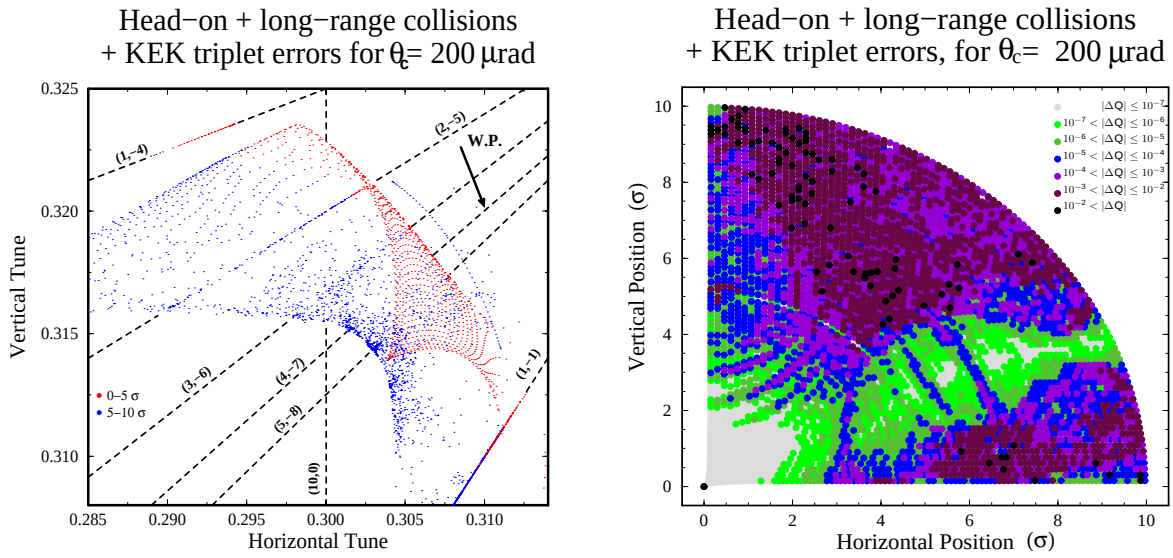

Figure 3: Tune footprint and diffusion map for a model including the head-on and long-range collision effect and the KEK triplet nonlinearities for a 200 μrad crossing angle. The symbols are the same as in Figs. 1 and 2.

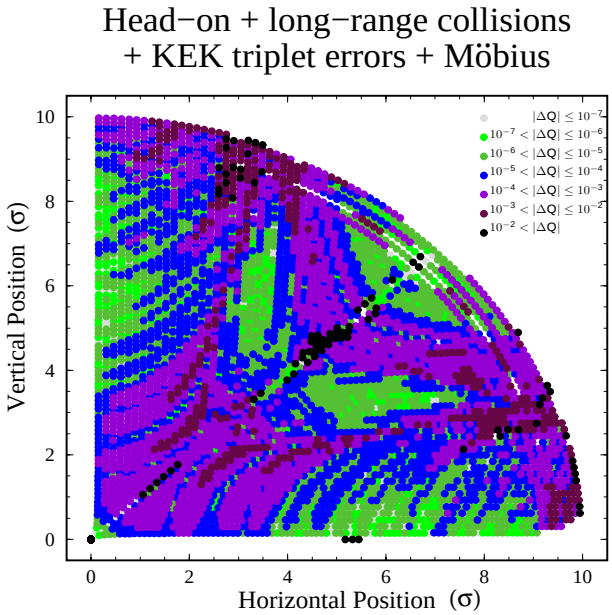

Figure 4: Diffusion map for a model including a Möbius twist. The symbols are the same as in Figs. 2.

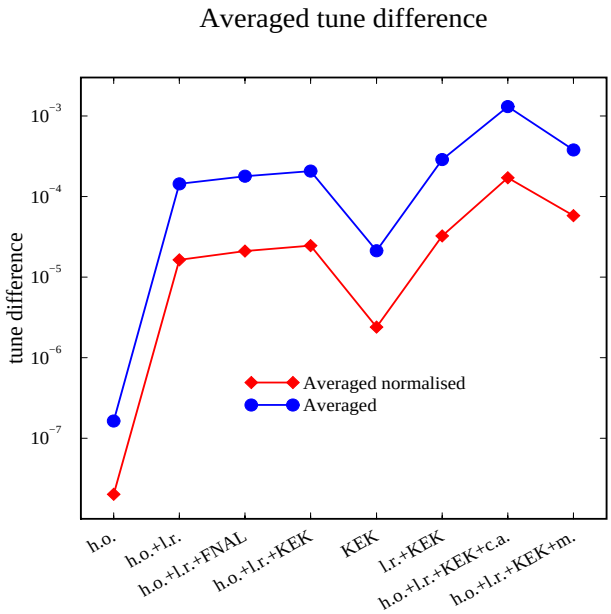

Figure 5: Averaged tune differences in logarithmic scale over all particle amplitudes and phases, for different models. The blue curve corresponds to a simple average of the tune change over all tracked particles and the red one to a normalised average by dividing the tune variation of every particle with its initial amplitude.

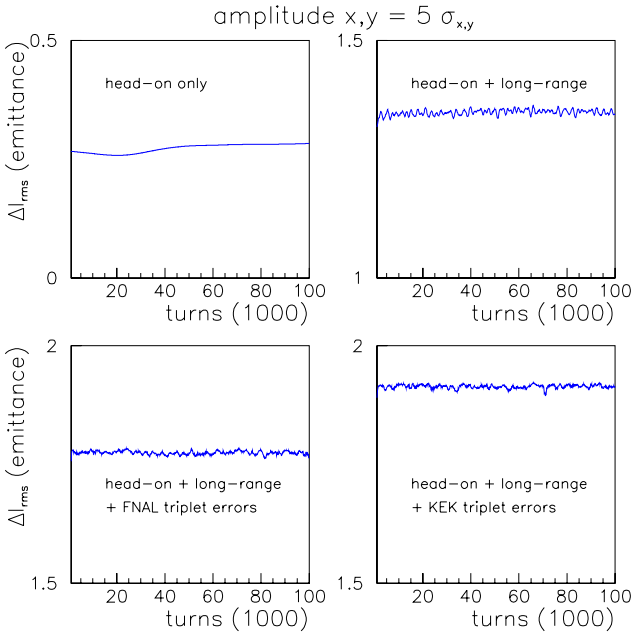

Figure 6: The variance in action (in units of rms emittance) for a group of 100 particles as a function of turn number. The particles were launched with identical transverse action corresponding to $5\sigma_{x,y}$ in both transverse planes and with random betatron phase. The figure demonstrates the effects of head-on collisions, long-range collisions and triplet nonlinearities, respectively.

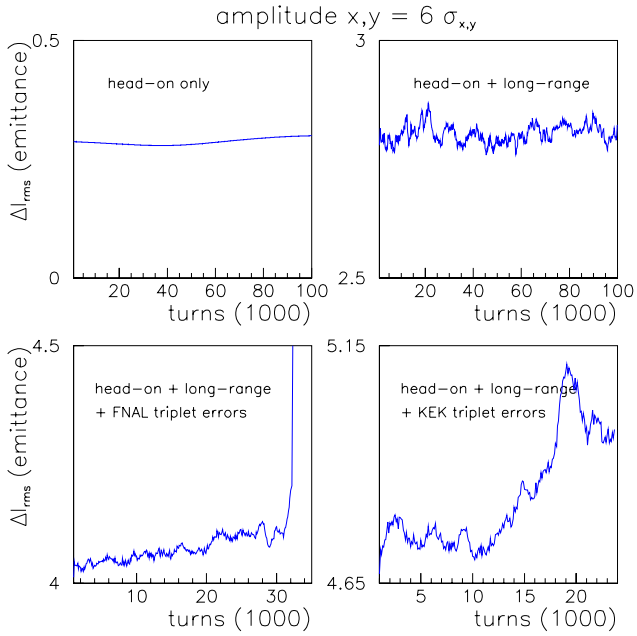

Figure 7: The variance in action (in units of rms emittance) for a group of 100 particles as a function of turn number. The particles were launched with identical transverse action corresponding to $6\sigma_{x,y}$ in both transverse planes and with random betatron phase. The figure demonstrates the effects of head-on collisions, long-range collisions and triplet nonlinearities, respectively.

3.2 Starting Amplitude

We study the evolution of the rms action spread for a group of particles, launched with random phases at the same values of transverse action. To suppress short-time fluctuations, *e.g.*, caused by static deformations of the invariant tori in phase space due to resonances, we compute the running average over 1000 turns of the rms action spread. The evolution of the rms spread at a starting amplitude of $5\sigma_{x,y}$ in both transverse planes is illustrated in Fig. 6, comparing the situation of head-on collisions only, with the cases of long-range collisions and triplet errors. In all pictures, the diffusion is quite limited. Thus, an amplitude of $5\sigma_{x,y}$ seems to lie inside the diffusive aperture.

Figure 7 shows a similar picture for a starting amplitude of $6\sigma_{x,y}$. While the head-on case looks comparable, the action spread shows notably larger variation when the long-range collisions are present. If the triplet errors are also switched on, some of the tracked particles experience a rapid growth in amplitude, leading to a steep growth in the calculated spread of action values. When the first particle is lost, we stop the simulation. This accounts for the much shorter time scale on the two bottom pictures.

More systematically, we can compute the diffusion at many different amplitudes and for each case compute the average increase in the rms action spread per turn. The result is illustrated in Fig. 8, which compares different combinations of head-on collisions, long-range interactions, triplet field errors, tune modulation, and Möbius twist. The tune modulation has little, if any, effect on the diffusion. The Möbius twist appears to increase the diffusion at low amplitudes, while the diffusion at larger amplitudes remains unaffected. In all cases including long-range collisions, there is a well defined diffusive aperture, between 5.5 and $6\sigma_{x,y}$, beyond which the motion is unstable. In the case of the SSC the equivalent limit without tune modulation was found to be between 6 and $7\sigma_{x,y}$ [1], a similar number (however, the long-range bunch separation was only $7.5\sigma_{x,y}$).

Figure 9 compares the diffusion generated by head-on plus long-range beam-beam interactions with that due to the uncorrected triplet field errors alone. The latter give rise to strong diffusion at an amplitude of about $8\sigma_{x,y}$, which is 2σ larger than for the beam-beam effect. The differences between FNAL and KEK field errors appear to be marginal.

We can use the tune variation of the tracked particles in order to confirm the established diffusive aperture thresholds. In Fig. 10, we plot the tune difference versus the amplitude, averaged over all initial $x-y$ amplitude ratios (a), and for a fixed ratio $\phi \equiv \arctan y/x = 45°$ corresponding to particles with equal initial positions (b), for the same cases as in Fig. 1. We also mark two thresholds corresponding to the precision boundary and to an empirical crude loss boundary for tune changes bigger than 10^{-4}. For all

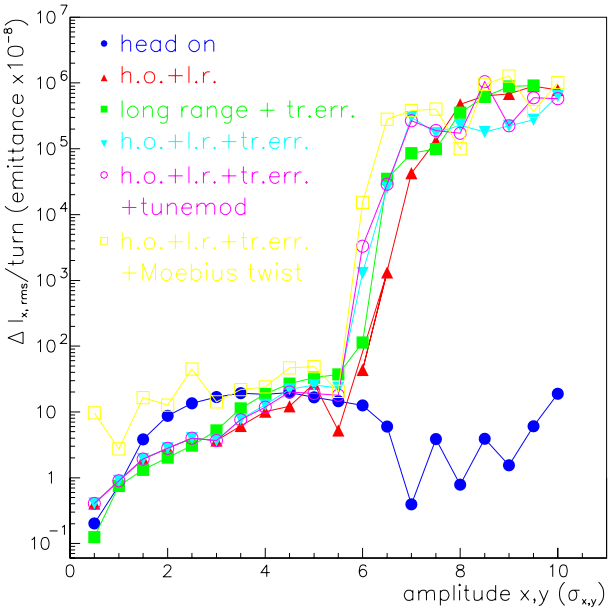

Figure 8: The change of action variance per turn as a function of the starting amplitude. Compared are the cases: head-on collisions only; head-on and long-range collisions; long-range collisions plus KEK triplet field errors; both types of collisions plus KEK triplet field errors; the additional effect of a tune modulation at the synchrotron frequency (22 Hz) of amplitude 10^{-4}; and the additional effect of a Möbius twist.

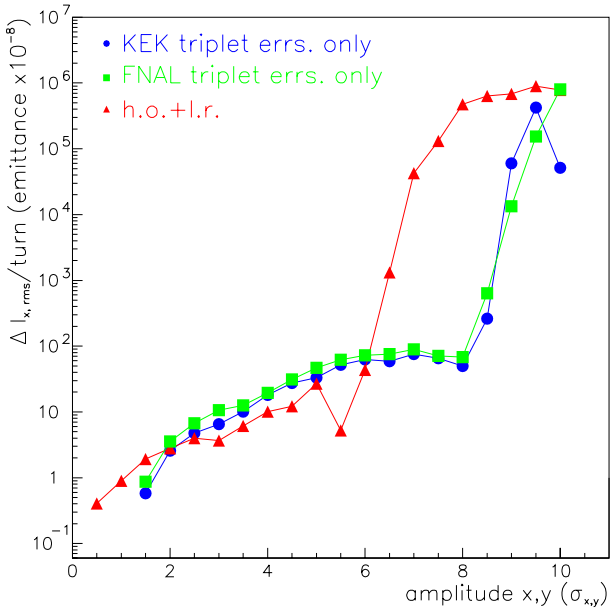

Figure 9: The change of action variance per turn as a function of the starting amplitude. Compared are the effect of beam-beam collisions with that of the KEK and FNAL triplet field errors.

the cases where long-range collisions and triplet field errors are included, the loss boundary is located at the same point, around $5.5\sigma_{x,y}$. For the case where the triplet field errors are not added to the beam-beam effect, the threshold is reached a little further, around $6\sigma_{x,y}$. The case with only the KEK triplets is clearly more stable, but indeed there is still a visible effect for larger initial amplitudes. No effect whatsoever can be observed for the head-on only case, where the tune variation is very close to the precision limit of the method.

The complementary picture (Fig. 10b) for a fixed initial amplitude ratio gives the same qualitative information regarding the dynamical influence of the various perturbations included in the model. The fluctuation of the tune variation with the initial amplitudes is due to the presence of some high order resonances which are identified and indicated in the plot.

In the following we study the dependence of the diffusion on various parameters. For simplicity, we choose a fixed launch amplitude of $5\sigma_{x,y}$ in both transverse directions, which is close to the limit of stability in the nominal case.

3.3 *Tune Scan*

Figure 11a presents the change of the action spread per turn as a function of the horizontal tune. The vertical tune was held constant and equal to 59.32. The nominal horizontal tune of $Q_x = 63.31$ is close to a valley. The highest peaks correspond to tunes close to the 3rd, 7th and 4th integer resonances. Figure 11b shows the result of another tune scan performed parallel to the tune space diagonal, *i.e.*, at a constant distance to the coupling resonance. This scan indicates that the nominal working point is close to optimal.

3.4 *Phase-Advance Scan*

Figure 12 demonstrates that a difference in horizontal phase advance between the two half arcs has little effect on the diffusion rate. Thus, the weak-strong beam-beam interaction does not constrain this parameter, which might be adjusted for optimum chromatic correction or for minimising strong-strong beam-beam effects.

3.5 *Offset*

We have also investigated the effect of a transverse offset between the two colliding beams. Figure 13 presents the change of the action spread per turn as a function of the horizontal amplitude for different values of horizontal separation at one of the two IPs. There is no noticeable effect for an offset varying from $0.2\sigma_{x,y}$ up to $2\sigma_{x,y}$.

3.6 *Beam Current*

Figure 14 depicts the effect of the bunch population on the diffusive aperture. We tracked particles with the same initial amplitude for 4 different bunch populations. The dependence of the difference between the diffusive aperture

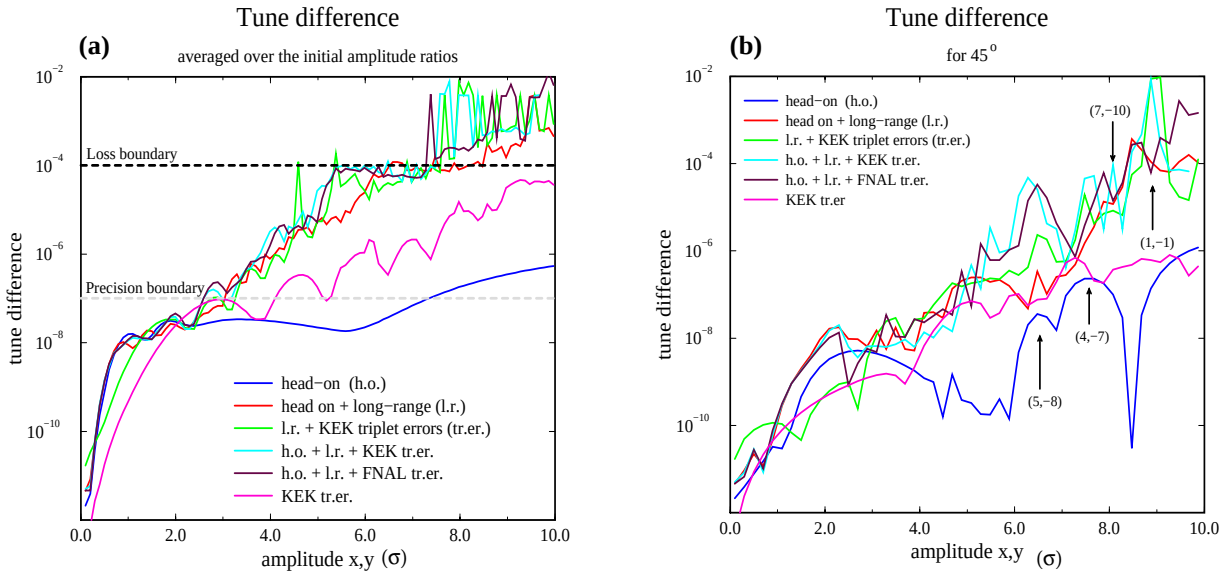

Figure 10: The change of frequency per 500 turns **(a)** averaged over all initial amplitude ratios $x - y$, and **(b)** for a fixed initial ratio of $45°$, as a function of the starting amplitude. Compared are the cases: head-on collisions only; head-on and long-range collisions; long-range collisions plus KEK triplet field errors; both types of collisions plus KEK triplet field errors; both types of collisions plus FNAL triplet field errors; only KEK triplet errors.

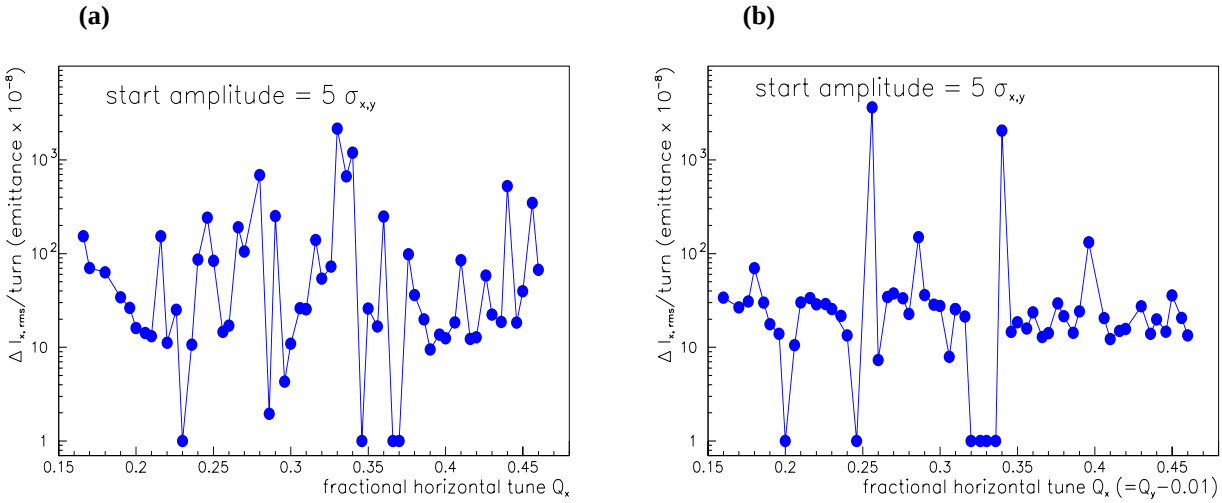

Figure 11: The change of action variance per turn (in units of rms emittance times 10^{-8}) as a function of the horizontal tune **(a)** for a constant vertical tune, and **(b)** for both the tunes varying so as to keep a constant distance to the $(1,-1)$ coupling resonance. The starting amplitude is 5σ in both planes.

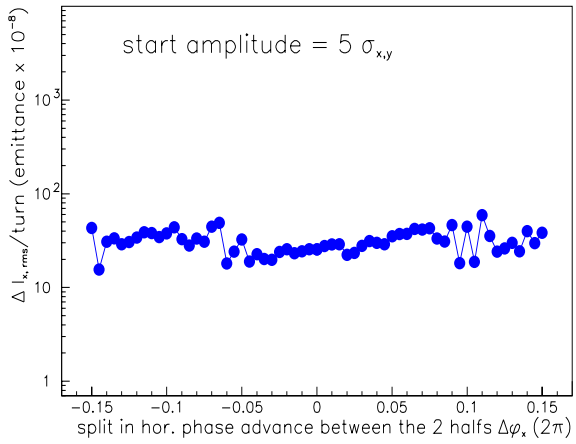

Figure 12: The change of action variance per turn (in units of rms emittance times 10^{-8}) as a function of the difference in horizontal phase advance between the two half arcs. The total horizontal tune is held constant, equal to the nominal. The vertical phase advance per arc is not changed.

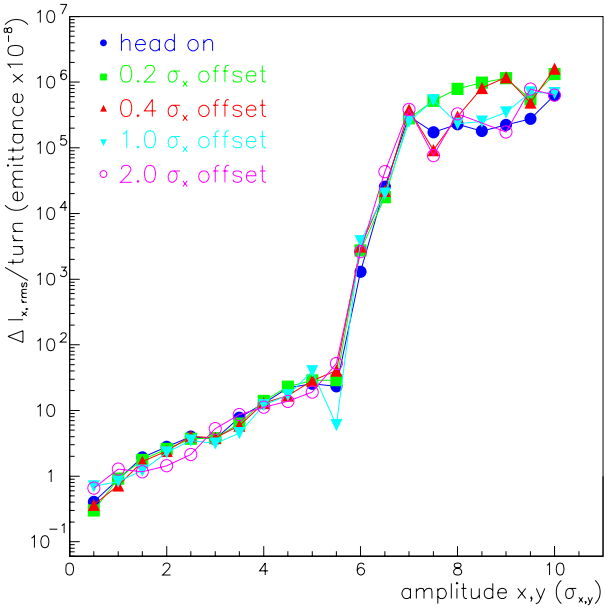

Figure 13: The change of action variance per turn (in units of rms emittance times 10^{-8}) as a function of the starting amplitude for different transverse offsets at one of the two main IPs.

and beam separation at the parasitic collision points on current follows the square root law found for the SSC, which is also expected from a simple scaling argument for a long-range force of the form $1/r$ [1].

3.7 Crossing Angle

Figure 15 shows a scan of the diffusion rate versus the crossing angle. For crossing angles smaller than 300 μrad, the diffusion increases by many orders of magnitude. The design crossing angle thus appears to be a good choice.

The tune variation averaged over initial amplitude ratios versus the initial amplitude for the two crossing angles of 300 and 200 μrad is displayed in Fig. 16. There is more than 1σ difference between the locations of the empirical loss boundary, for the two cases.

3.8 $\beta^\star$ Scan

Figure 17 depicts the dependence of the diffusion on the IP beta function. The crossing angle θ_c was varied simultaneously with the beta function so as to maintain a constant value of $\theta_c/\theta_{x,y}$, *i.e.*, a constant separation at the parasitic collision points. The figure indicates a minimum acceptable beta function of about 0.35 m, below which the diffusion at $5\sigma_{x,y}$ becomes prohibitively large, for uncorrected triplet errors.

4 CONCLUSIONS

We have performed a series of weak-strong beam-beam simulations for the LHC. The simulation model is similar to the approach followed by John Irwin for the SSC [1], studying the diffusion in the action variable of a group of particles launched at the same transverse amplitude with random betatron phase. We added some new features, such as a Möbius twist element, and the tracking data was further processed by a frequency map analysis.

Preliminary simulation results indicate that the stability of particle motion is completely determined by the long-range beam-beam interaction, which causes substantial diffusion at amplitudes beyond about $6\sigma_{x,y}$. If triplet nonlinearities are also taken into account, unstable particles at these amplitudes can be lost within a few 10000 turns, while without triplet errors no particle loss is observed within the first 10^5 turns. In the presence of long-range collisions, the simulation results for the FNAL and the KEK triplet errors are almost indistinguishable in the action and small in the average tune changes. The uncorrected triplet field errors alone cause a strong diffusion at a threshold amplitude of about $8\sigma_{x,y}$, i.e. 2σ larger than for the long-range collisions. Compared with both long-range interactions and triplet errors, the effect of the head-on collisions is negligible. A tune modulation of amplitude 10^{-4} at 22 Hz has only marginal effect on the diffusion. Equally small effect has a transverse offset between the two beams in one of the head-on collisions. With long-range collisions present, the diffusive aperture of about $6\sigma_{x,y}$ is 3.5σ smaller than the beam-beam separation at the parasitic collision points. The distance between the diffusive aperture and the beam-beam separation increases as the square root of the bunch population, in accordance with previous studies [1].

The present nominal working point in the tune diagram corresponds to a broad local minimum in the diffusion rate calculated for a starting amplitude of $5\sigma_{x,y}$. The diffusion rate is unaffected by a difference in the horizontal phase advance between the two IPs. For crossing angles below

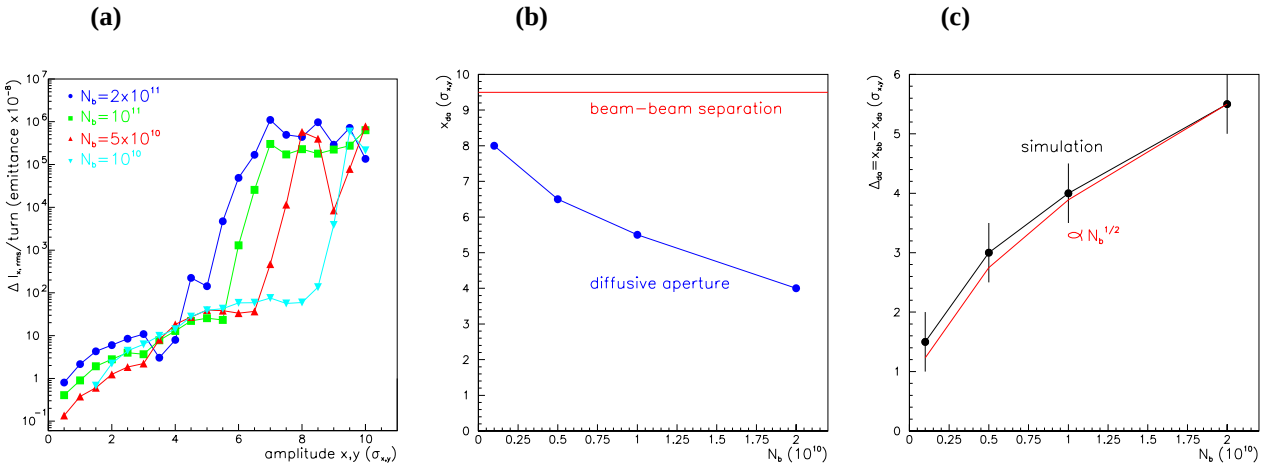

Figure 14: Dependence of diffusion due to long-range collisions on the beam current: **(a)** the change of action variance per turn as a function of the bunch population; **(b)** approximate diffusive aperture as a function of the bunch population; **(c)** same as the left picture, but the vertical axis is the distance to the other beam at the parasitic collision point; a square root dependence is also indicated for comparison.

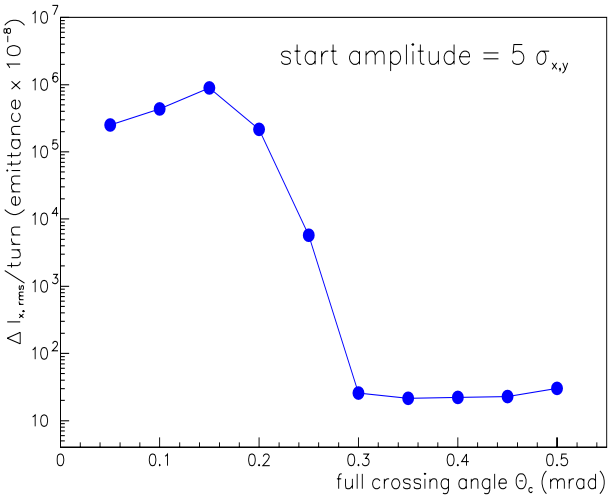

Figure 15: The change of action variance per turn as a function of the full crossing angle. The start amplitude is $5\sigma_{x,y}$ in both planes. The vertical axis gives the variance in units of the design rms emittance times 10^{-8}.

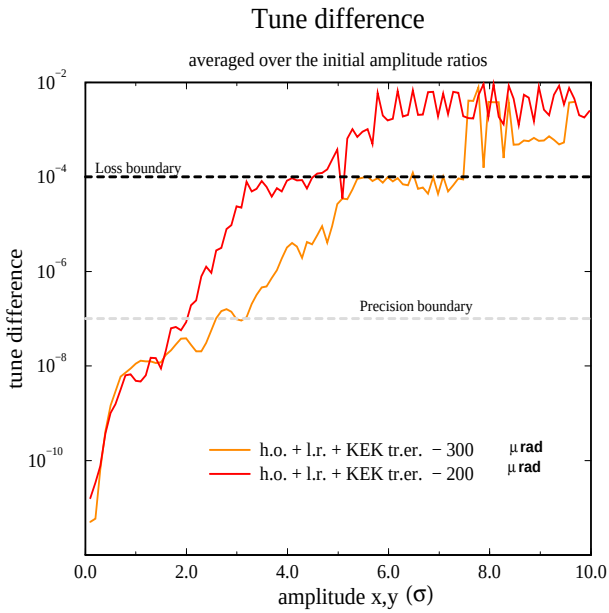

Figure 16: The tune variation per 500 turns averaged over the initial $x - y$ amplitude ratio, for two different crossing angles of 300 and 200 μrad.

250 μrad the diffusion at $5\sigma_{x,y}$ increases by many orders of magnitude. For large crossing angles, the diffusion is roughly constant. Therefore, the design crossing angle of 300 μrad appears to be optimal. Finally, the IP beta function could be squeezed down to about 0.35 m without appreciable increase in the diffusion rate at $5\sigma_{x,y}$. For even smaller values of $\beta^{\star}_{x,y}$ the $5\sigma_{x,y}$ diffusion rate increases dramatically, if the triplet errors remain uncorrected. At $\beta^{\star}_{x,y} = 0.25$ m there is strong diffusion below 4σ.

5 ACKNOWLEDGEMENT

We thank J. Gareyte, H. Grote, J.-P. Koutchouk, F. Ruggiero and F. Schmidt for helpful discussions and information.

6 REFERENCES

[1] J. Irwin, "Diffusive Losses from SSC Particle Bunches due to Long-Range Beam-Beam Interactions", SSC-223 (1989).

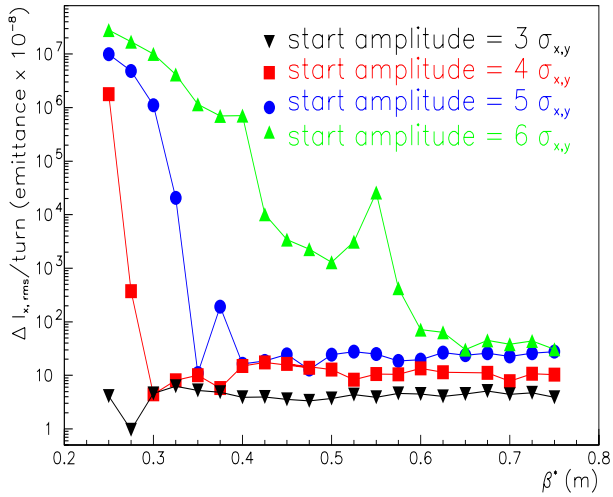

Figure 17: The change of action variance per turn as a function of $\beta^{\star}_{x,y}$. Along with $\beta^{\star}_{x,y}$, the crossing angle is changed, so as to maintain a constant ratio $\theta_c/\theta_{x,y}$. The starting amplitude in both planes varies from 3 to $6\sigma_{x,y}$. The vertical axis gives the variance in units of the design rms emittance times 10^{-8}.

[2] The LHC Study Group, "LHC The Large Hadron Collider, Conceptual Design", CERN/AC/95-05 (1995).

[3] W. Chou and D. Ritson, "Dynamic Aperture Studies During Collisions in the LHC", IEEE PAC 1997, Vancouver (1997).

[4] W. Herr, "Beam-beam effects in the LHC", *CERN SL report 94-92 (AP) - LHC Note 301* (1994).

[5] FNAL High Gradient Quad MQXB, reference harmonics at collision, October 27, 1998, updated Dec 7, 1998; on the worldwide web (FNAL LHC pages).

[6] H. Grote, private communication (1999).

[7] N. Ohuchi, K. Tsuchiya, T. Ogitsu, Y. Ajima, M. Qiu, A. Yamamoto, T. Shintomi, "Magnetic Field Measurements of a 1-m Long Model Quadrupole Magnet for the LHC Interaction Region", KEK Preprint 98-167 (1998).

[8] R. Talman, "The Möbius Accelerator", CLNS-94-1300 (1994).

[9] R. Bartolini and F. Schmidt, "Normal Form via Tracking or Beam Data", Part. Acc. 59, p. 93 (1998).

[10] J. Laskar, Physica D 67, 257 (1993); J. Laskar and D. Robin, Part. Acc. 54, 183 (1996).

[11] Y. Papaphilippou, "Frequency Maps of LHC Models", presented at IEEE PAC99, New York (1999).

[12] J. Laskar, "Introduction to Frequency Map Analysis", NATO-ASI, S'Agaro, Spain, unpublished (1995).

[13] S. Henderson, M. Billing, R. Holtzapple, R. Littauer, B. McDaniel, D. Rice, D. Rubin, D. Sagan, R. Talman and A. Temnyck, "Investigation of the Möbius accelerator at CESR", presented at IEEE PAC99, New York (1999).